

Nanoeutectic Composites: Processing, Microstructure and Properties

J. Das¹ · T. Maity¹ · A. Singh¹

Received: 30 June 2015 / Accepted: 25 August 2015 / Published online: 1017
© The Indian Institute of Metals - IIM 2015

Abstract Nanostructured alloys exhibit high strength and large elastic strain limit. Unfortunately, the plasticity of these alloys is disappointingly low at room temperature than that of the coarse grain counterparts. In this work, a series of nanoeutectic composites have been developed in Ti–Fe and Ni–Zr based alloys, which exhibit very high strength, like bulk metallic glasses and large plasticity at room temperature. Systematic investigations have been performed to reveal the effect of alloy addition on the alteration of the microstructure and the properties of nanolamellar phases. Even though, in some cases, alloy addition stabilizes micrometer-sized proeutectic bcc/fcc solid solution phase(s) with dendritic morphology, but the residual melt solidifies into a binary nanoeutectic comprised of alternating soft bcc/fcc phase together with hard intermetallic phase. Furthermore, electron microscopic studies of differently deformed specimens and strain rate jump test have been performed to reveal the role of eutectic lamellae on the strain rate sensitivity and to explore the origin of plasticity in nanoeutectic composites.

Keywords Ti-alloys · Ni-alloys · Nanoeutectic · Transmission electron microscopy · Deformation mechanism

1 Introduction

The eutectic alloys have found wide engineering applications for making direct cast products due their low melting temperature and good castability. The lamellar composite microstructure, comprising of alternate soft solid solution and hard intermetallic phases, offers tunable mechanical properties. Such in situ composites exhibit very high strength than their constituent single-phase alloys due to their finer lamellae thickness ($\sim 1 \mu\text{m}$). However, supersaturation in the eutectic lamellae phases and small dislocation mean free path under strong constraining effect provided by the lamellae, result poor ductility and deteriorate the mechanical properties. Usually, bulk metallic glass forming compositions lie close to the deep stable/metastable eutectic compositions. Therefore, these alloys eventually solidify into eutectic microstructure upon slow cooling.

Woodcock reported that, addition of Nb/Ta/Mo to multicomponent Ti–Cu–Ni–Sn glass forming compositions stabilizes the primary β -Ti solid solution phase in the undercooled liquid [1]. Furthermore, slow cooling, assists chemical partitioning of the alloy constituents, and the composition of the residual melt become enriched in solute content towards solidification into lamellar eutectic microstructure [2]. On the other hand, high degree of constitutional undercooling produces large nucleation rate, whereas, the growth of the eutectic phases become restricted within sub-micrometer scale towards the synthesis of nano-eutectic composites (NECs) [3].

Along this line, attempts has been made to produce binary eutectic composites with reduced lamellar spacing through arc melting and subsequent solidification at a low cooling rate (10 K/s) [4, 5], as well as their microstructure modification upon alloy additions. Similarly, bulk Ti–Fe–

✉ J. Das
j.das@metal.iitkgp.ernet.in

¹ Department of Metallurgical and Materials Engineering,
Indian Institute of Technology Kharagpur, Kharagpur
721302, West Bengal, India

(Sn) NECs with FeTi and metastable β -Ti lamellae in their microstructure have been developed [6–8]. However, it was reported that addition of Sn refined the eutectic lamellar spacing of $\text{Ti}_{70.5}\text{Fe}_{29.5}$ and improved plasticity [4]. On the other hand, Park et al. [9] developed Ni-8Zr nano-eutectic matrix composites comprising of proeutectic micrometer sized γ -Ni reinforced NEC through in situ suction casting to obtain 2 mm diameter rod. The material showed high yield strength of 1827 MPa and 22 % plastic strain. The improved plasticity of these composites was correlated to the formation of shear bands in the matrix and the dislocation slip in the γ -Ni dendrites [9].

In the present work, the effect of alloy additions on the microstructure and deformation behavior of Ti–Fe–(Sn) and Ni–Zr–(Al) nano-lamellar eutectic composites have been reported. The role of lamellar phases on the strain rate sensitivity and the slip transfer across the lamellae interface upon deformation, have been explored.

2 Methods of Processing and Characterization

Two different alloy system such as $(\text{Ti}_{0.705}\text{Fe}_{0.295})_{100-x}\text{Sn}_x$ ($x = 0, 2, 3$), and $(\text{Ni}_{0.912}\text{Zr}_{0.088})_{100-y}\text{Al}_y$ ($y = 0, 1$) were studied. The investigated alloy specimens were prepared by arc-melting of the pure elements. The processing of arc melted ingots (AMI) involved preparation of binary eutectic alloys of $\text{Ti}_{70.5}\text{Fe}_{29.5}$, and $\text{Ni}_{91.2}\text{Zr}_{8.8}$, followed by alloy additions such as, Sn or Al to achieve the desired compositions. The composition of the AMI was verified by chemical analysis using energy dispersive X-ray spectroscopy (EDS). Apart from the above mentioned compositions, the constituent single phases present in Ti–Fe–(Sn) denoted as microcrystalline single phase(MSP) alloys, such as $\text{Ti}_{80}\text{Fe}_{20}$, $\text{Ti}_{51.5}\text{Fe}_{48.5}$ and $\text{Ti}_{82}\text{Fe}_{10}\text{Sn}_8$ were prepared. Similarly, the constituent single phases present in the Ni–Zr–(Al) AMI composites, such as, Ni_5Zr MSP, Ni MSP, and $\text{Ni}_{95}\text{Zr}_{0.4}\text{Al}_{4.6}$ MSP were prepared also [10, 11]. Nominal alloy composition of AMIs $(\text{Ti}_{0.705}\text{Fe}_{0.295})_{100-x}\text{Sn}_x$ ($x = 0, 2, 3$) and $(\text{Ni}_{0.912}\text{Zr}_{0.088})_{100-y}\text{Al}_y$ ($y = 0, 1$), and

the constituent single phases present in the eutectic composites, which are denoted as microcrystalline single phase (MSP) alloys, are summarized in Table 1. Samples were cut from AMI, and MSP specimens using an electro-discharge machine (EDM). The samples were metallographically polished using 9 μm down to 1 μm particle size diamond suspension. Final polishing was performed using colloidal-silica suspension for microstructure characterization. A high resolution X-ray diffraction (XRD) unit (Philips PANalytical PW 3373, Holland) with Cu-K α radiation was used for structural investigation. A ZEISS EVO 60, Japan scanning electron microscopy (SEM) equipped with an energy dispersive X-ray spectrometer (EDS Oxford ISIS 300) was used for investigating the microstructures of the composites. The detailed structural investigations were carried out using a high resolution transmission electron microscope (HRTEM, JEOL JEM 2100, Japan). For TEM investigation, thin slices were cut and were thinned using precision ion polishing system (Gatan PIPS-691) with liquid N_2 cooling facility. Wide polishing techniques were used for obtaining an electron transparent region for TEM sample preparation. Parallelepiped compressive specimens with a specimen aspect ratio of 2:1 were prepared using electro-discharge machining (EDM). All the surfaces of the test specimens were polished using colloidal-silica prior to compression test to reveal the deformation morphology. The compression tests were performed using TINIUS Olsen H50KS universal testing machine at an initial strain rate of $8 \times 10^{-4}/\text{s}$ at room temperature. Furthermore, strain rate jump tests were carried out to determine the strain rate sensitivity of the composites at different strain rates of $8 \times 10^{-5}/\text{s}$, $8 \times 10^{-4}/\text{s}$, and $8 \times 10^{-3}/\text{s}$, at room temperature according to the ASTM G129-00 standard [12]. Data points were used only after yielding in the steady-state plastic flow regime [13]. Vickers hardness was measured using a Vickers bulk hardness tester (Leco LV-700, USA) at 20 kg load for 15 s dwell time. Minimum 20 indentations were made at each indentation load to obtain representative hardness values of the AMIs and MSPs.

Table 1 Nominal alloy composition of arc melted ingots (AMI) of $(\text{Ti}_{0.705}\text{Fe}_{0.295})_{100-x}\text{Sn}_x$ ($x = 0, 2, 3$) and $(\text{Ni}_{0.912}\text{Zr}_{0.088})_{100-y}\text{Al}_y$ ($y = 0, 1$), and their constituent single phases present in the eutectic composites, which are denoted as microcrystalline single phase (MSP) alloys

Alloy composition (phase)	Sample code	Alloy composition (phase)	Sample code
$\text{Ti}_{70.5}\text{Fe}_{29.5}$ (β -Ti+FeTi)	$x = 0$ AMI	$\text{Ni}_{91.2}\text{Zr}_{8.8}$ (γ -Ni+ Ni_5Zr)	$y = 0$ AMI
$\text{Ti}_{69.09}\text{Fe}_{28.91}\text{Sn}_2$ (β -Ti+FeTi)	$x = 2$ AMI	$\text{Ni}_{90.29}\text{Zr}_{8.71}\text{Al}_1$ (γ -Ni+ Ni_5Zr)	$y = 1$ AMI
$\text{Ti}_{68.39}\text{Fe}_{28.61}\text{Sn}_3$ (β -Ti+FeTi)	$x = 3$ AMI		
$\text{Ti}_{80}\text{Fe}_{20}$ (β -Ti)	$\text{Ti}_{80}\text{Fe}_{20}$ MSP	$\text{Ni}_{95}\text{Zr}_{0.4}\text{Al}_{4.6}$ (γ -Ni)	$\text{Ni}_{95}\text{Zr}_{0.4}\text{Al}_{4.6}$ MSP
$\text{Ti}_{82}\text{Fe}_{10}\text{Sn}_8$ (β -Ti)	$\text{Ti}_{82}\text{Fe}_{10}\text{Sn}_8$ MSP	Ni_5Zr (Ni_5Zr)	Ni_5Zr MSP
$\text{Ti}_{51.5}\text{Fe}_{48.5}$ (FeTi)	$\text{Ti}_{51.5}\text{Fe}_{48.5}$ MSP	Pure-Ni (γ -Ni)	Ni MSP

3 Results and Discussion

3.1 Microstructure and Length Scale of the Constituent Phases

The XRD patterns of Ti–Fe–(Sn) composites display the presence of diffraction peaks of bcc β -Ti (I–3 m) and intermetallic FeTi (P–3 m) phases, whereas, Ni–Zr–(Al) composites show the presence of fcc γ -Ni (F–3 m) and intermetallic ordered fcc Ni₅Zr (F–43 m) phases. As for example, XRD patterns of $x = 3$ AMI and $y = 1$ AMI are shown in Fig. 1. The lattice parameter (a) of the individual phases have been determined by the Rietveld refinement method [14]. The a values of the β -Ti ($a_{\beta\text{-Ti}}$) phase varies from 0.3200 nm ($x = 0$ AMI) to 0.3255 nm ($x = 3$ AMI), whereas, the value of a_{FeTi} remains almost constant at 0.2998 nm, in the various Sn containing composites [10, 15]. Similarly, $a_{\gamma\text{-Ni}}$ increases with addition of Al in Ni–Zr–(Al) composites from 0.3527 nm ($y = 0$ AMI) to 0.3531 nm ($y = 1$ AMI), however, the value of $a_{\text{Ni}_5\text{Zr}}$ remains almost constant at 0.6706 nm. The investigation clearly reveals that Ti and Al preferably dissolves in β -Ti and γ -Ni phases, respectively, due to the solubility differences of Sn and Al in β -Ti/FeTi and γ -Ni/Ni₅Zr phases. On the other hand, XRD pattern of Ti₈₀Fe₂₀ MSP and Ti₈₂Fe₁₀Sn₈ MSP have revealed the peaks of β -Ti phase, whereas, peaks of FeTi have been identified in the case of Ti_{51.5}Fe_{48.5} MSP. Similarly, the XRD patterns of Ni MSP and Ni₉₅Zr_{0.8}Al_{4.6} MSP reveals the presence of γ -Ni phase only as listed in Table 1. Whereas, XRD peaks of Ni₅Zr phase has been identified in case of Ni₅Zr MSP.

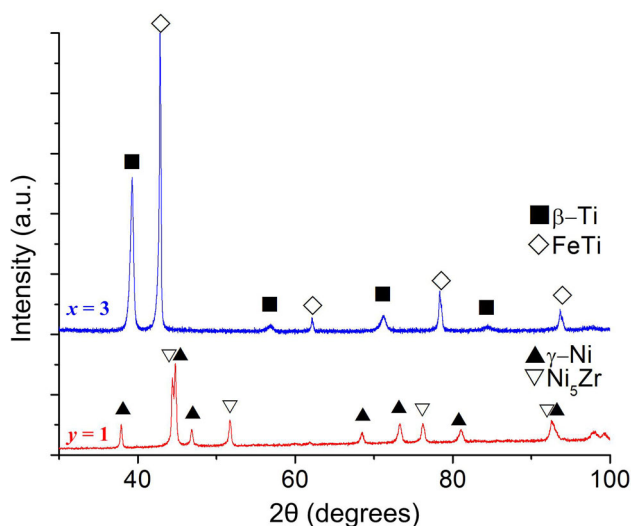


Fig. 1 XRD patterns of $x = 3$ AMI and $y = 1$ AMI showing diffraction peaks from β -Ti+FeTi and γ -Ni+Ni₅Zr phases, respectively

The SEM micrograph of $x = 3$ AMI exhibits a homogeneous nano-lamellar eutectic microstructure without any trace of pro-eutectic phase(s), as shown in Fig. 2a. The EDS analysis reveals the brighter lamellae phase to be rich in Fe than that of the darker matrix. EDS analysis of $x = 0$ AMI reveals the composition of the bright lamellar phase to be Ti₅₂Fe₄₈ and the darker matrix to be Ti₈₀Fe₂₀, which are identified as FeTi and β -Ti phases, respectively. On the other hand, the EDS analysis of $x = 3$ reveals the composition of dark and bright contrast phases to be Ti₈₂Fe_{10.5}Sn_{7.5} and Ti_{51.5}Fe_{48.5}, respectively. The microstructure of $y = 1$ AMI, as shown in Fig. 2b, shows the presence of alternate nano-lamellae of dark and bright contrast of γ -Ni and Ni₅Zr phases showing eutectic morphology, with 2.5 ± 0.5 vol% of pro-eutectic γ -Ni phase with dendritic morphology. The average lamellar thickness (λ_e) has been estimated by measuring their values at 20 different locations around the center of the AMI and is found to decrease from 800 ± 50 nm in $x = 0$ AMI, down to 330 ± 20 nm in $x = 3$ AMI composites, respectively. On the other hand, λ_e is estimated to be 270 ± 20 nm in $y = 0$ AMI and 240 ± 15 nm in $y = 1$ AMI composites. Thereby, it is observed that the ternary alloy additions like Sn and Al, refines the lamellar spacing in the NECs.

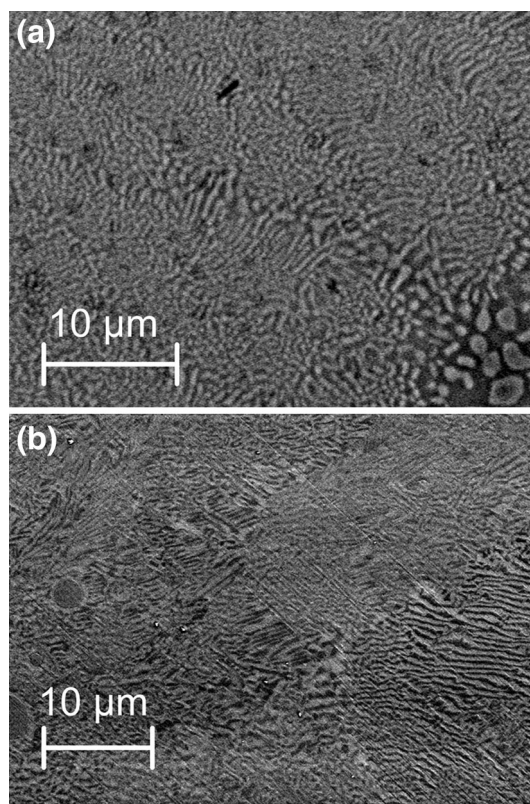


Fig. 2 SEM images showing the evolution of homogeneous nano-lamellar eutectic microstructure in **a** $x = 3$ AMI and **b** $y = 1$ AMI

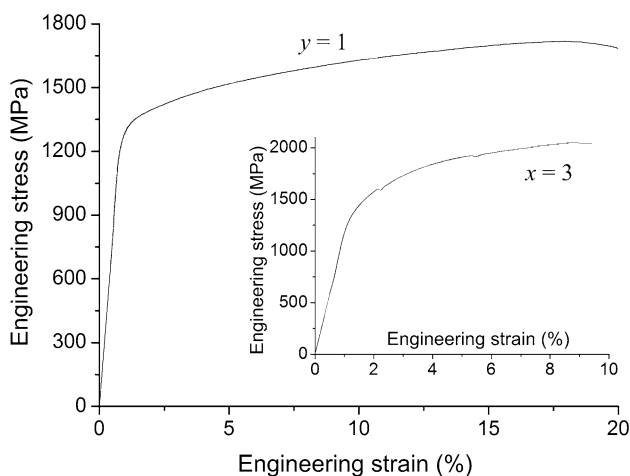


Fig. 3 The engineering stress–strain curves of $y = 1$ AMI and *inset* $x = 3$ AMI NECs at an initial strain rate of 8×10^{-4} /s showing high strength and large plasticity

3.2 Mechanical Properties Under Compression and Strain Rate Sensitivity

Compression test has been carried out to reveal the bulk mechanical properties of the NECs under unconstrained geometry at room temperature. Figure 3 shows the engineering stress–strain curves of $x = 3$ AMI and $y = 1$ AMI NECs, respectively. The $x = 3$ AMI composite exhibits high value of yield strength (σ_y) ~ 1420 MPa, ultimate compressive strength (σ_{max}) ~ 2040 MPa, with 10 % plastic strain ε_p . Similar observation has been reported earlier for different Sn containing Ti–Fe–(Sn) AMI NECs [6]. On the other hand, $y = 0$ AMI and $y = 1$ AMI NECs exhibit $\sigma_y = 1346$ and 1305 MPa, $\sigma_{max} = 1880$ and 1720 MPa, with improved $\varepsilon_p = 26$ and 20 %, respectively. It has been observed that all the NECs exhibit a strong strain hardening behavior.

The strain rate jump test has been performed to estimate the strain rate sensitivity (m) of the NECs at room temperature. Figure 4a, b shows the true stress–true strain curves of the $x = 2$ AMI and $y = 1$ AMI NECs under compression, showing two successive strain rate jumps from 8×10^{-5} /s to 8×10^{-4} /s (jump 1) and from 8×10^{-4} /s to 8×10^{-3} /s (jump 2). In the present investigation, jumps from a lower strain rate to a higher strain rate has been adopted in order to avoid the deleterious effect of machine compliance during down-jump and to make the dataset free from errors [16]. The strain rate sensitivity (m) and the activation volume (V^*) of the tested specimens have been determined from these stress overshoot according to the following equation [13]:

$$m = \frac{\ln\left(\frac{\sigma_1}{\sigma_2}\right)}{\ln\left(\frac{\dot{\varepsilon}_1}{\dot{\varepsilon}_2}\right)} \quad (1)$$

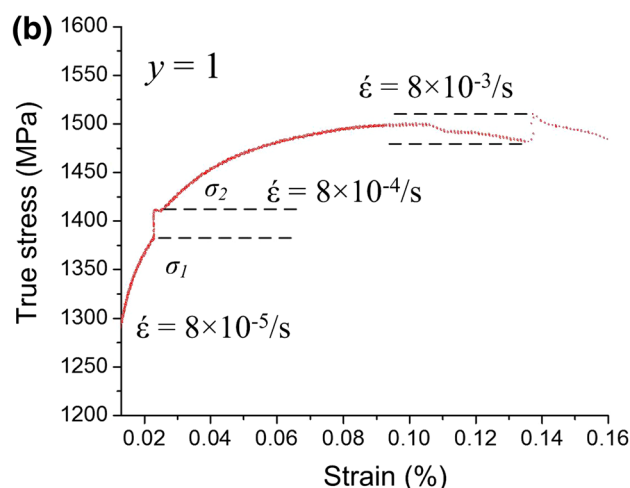
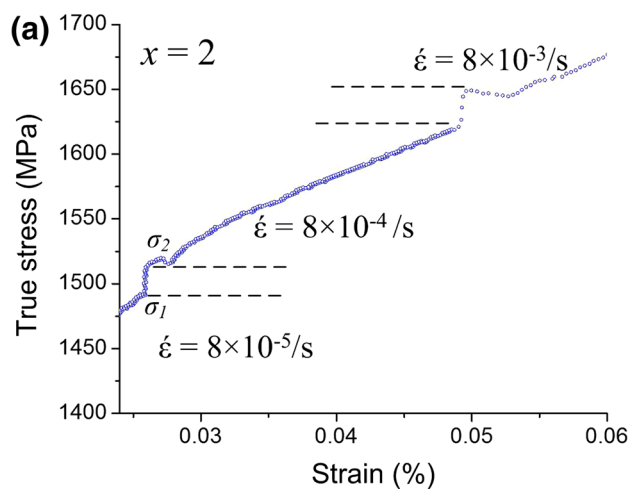


Fig. 4 True stress–true strain plots of **a** $x = 2$ AMI and **b** $y = 1$ AMI for determining the strain rate sensitivity (m) of the NECs showing the stress overshoot during strain rate jump

where, σ_1 and σ_2 corresponds to the stress overshoot at same strain, $\varepsilon = \varepsilon_0$ for a given strain rate jump from ε_1 to ε_2 , respectively, as depicted in Fig. 4.

In case of $x = 2$ AMI NEC, the value of σ_1 and σ_2 have been estimated to be 1529 and 1556 MPa for the jump 1, whereas, the values of σ_1 and σ_2 have been estimated to be 1701 and 1732 MPa for the jump 2, as shown in the true stress–strain curves in Fig. 4. The m values has been estimated to be $m = 0.0066$ and $m = 0.0074$, for $x = 2$ AMI NEC. Similarly, for $y = 1$ AMI NEC, the m values has been estimated to be $m = 0.00905$ and $m = 0.00828$. The activation volume (V^*) for deformation has been derived from these m values as [17]:

$$V^* = \sqrt{3} \frac{k_B T}{m \sigma} \quad (2)$$

where, σ is the yield strength at room temperature T (298 K) and K_B is the Boltzmann's constant. The V^* is

expressed in terms of b^3 , where b is the burgers vector of β -Ti in $x = 2$ AMI ($b = 0.2802$ nm) and γ -Ni in $y = 1$ AMI ($b = 0.2496$ nm). The V^* has been estimated to be $23b^3$ for $x = 2$ AMI and $40b^3$ for $y = 1$ AMI NECs.

The estimated V^* values of both $x = 2$ AMI and $y = 1$ AMI clearly indicates that higher rate dependence is associated with the lower V^* in the investigated NECs. The values of m and V^* of the $x = 2$ AMI is near similar to that ($m = 0.0086$ and $V^* = 22b^3$) measured by the nanoindentation investigation at constant loading rate experiments [18]. However, these V^* values are smaller than that of the coarse lamellar Pb–Sn eutectic ($V^* \sim 1000 \text{ \AA}^3$) [19], which clearly indicates the formation of sub-boundaries and large dislocation density in the lamellae interfaces, which reduces the dislocation mean free path. It has been reported that the V^* of the MSP specimens are $32b^3$, $26b^3$, and $39b^3$ for $\text{Ti}_{80}\text{Fe}_{20}$, $\text{Ti}_{82}\text{Fe}_{10}\text{Sn}_8$ and $\text{Ti}_{51.5}\text{Fe}_{48.5}$ MSPs, respectively. Therefore, the values V^* of the Ti–Fe–(Sn) MSPs are higher than that of NECs, due to their large grain size ($d = 50$ – 100 \mu m) in MSPs and narrow lamellae width of <330 nm [18]. Moreover, similar m values for Ti–Fe–(Sn) and Ni–Zr–(Al) specimens, as estimated by the strain rate jump test under bulk compression test and nanoindentation tests [18], indicates the similar mode of deformation mechanism to be operative in NECs.

3.3 Deformation Mechanism of Nano-lamellar Eutectic Composites

In order to explore the deformation mechanism in NECs, a few $x = 3$ AMI and $y = 1$ AMI specimens were deformed under compression at a strain rate of 8×10^{-4} /s up to 10 and 20 % plastic strain ϵ_p . The surfaces of the specimens were mirror polished prior to SEM investigation to study the evolution of deformation bands, geometry of slip in the nano-lamellar phases and their role during plastic deformation. Figures 5a, b show the surface features, as evolved on deformed $x = 3$ AMI ($\epsilon_p = 10$ %) and $y = 1$ AMI ($\epsilon_p = 20$ %), respectively. Figure 5a shows the formation of profuse slip bands in the β -Ti and FeTi lamellae phases, aligned at an angle of 90° and 45° – 55° in FeTi and β -Ti, respectively. Similarly, traces of large amount of profuse slip bands have been identified both in γ -Ni and Ni_5Zr nano-lamellar phases as marked by arrows in Fig. 5b. Since the growth direction of γ -Ni and Ni_5Zr is found to be similar along [100] direction, similar to β -Ti/FeTi in Ti–Fe–(Sn) NECs [4], therefore, preferred orientation of the slip lines with the growth direction of the lamellae, has been observed. No micro-/nanometer sized crack has been observed at the lamellae interfaces, which indicates that the lamellae interfaces are strong enough to slip transfer across the γ -Ni/ Ni_5Zr interfaces without any local failure.

However, long shear bands with large shear offset appear to pass across the specimen surface as shown in Fig. 5b. On the other hand, the profuse slip lines in γ -Ni dendrites has also been reported earlier [11], which has occurred due to the movement of dislocations, their multiplications and their mutual interactions contributing strain hardening in the bimodal composites. Moreover, arrest of propagating shear bands by the soft γ -Ni-dendrites assists large deformation of the nanoeutectic matrix in proeutectic dendritic Ni–Zr–(Al) NECs [11]. The TEM bright field (BF) images of deformed $x = 3$ AMI and $y = 1$ AMI NECs are shown in Fig. 5c, d, respectively. The presence of high-density slip lines all over the microstructure and dislocation pile-ups at the β -Ti/FeTi or γ -Ni/ Ni_5Zr lamellae interfaces indicate that dislocation slips and their pile-ups are the major source of work hardening in the NECs.

Usually, the plastic deformation proceeds with the slip transfer between the neighboring grains by suppressing the crack formation at the interface. Therefore, pile-up of dislocations in β -Ti or γ -Ni lamellae phase will either activate slip or cleavage in the adjacent FeTi or Ni_5Zr lamellae, respectively. On the other hand, the overall strength of the composite can be predicted from rule of mixture of the individual eutectic lamellar phases and by considering the lamellae refinement using Hall–Petch equation. Maity et al. [11, 15] have shown that the predicted strength values are very close to that of the measured hardness values of Ti–Fe–(Sn) and Ni–Zr–(Al) NECs, as reported earlier. The critical resolved shear stress (CRSS) value of the individual lamellar phases in $x = 0$ AMI and $x = 3$ AMI NECs, such as, $\text{Ti}_{80}\text{Fe}_{20}$ MSP [β -Ti(Fe) phase], $\text{Ti}_{51.5}\text{Fe}_{48.5}$ MSP [FeTi phase] and $\text{Ti}_{82}\text{Fe}_{10}\text{Sn}_8$ MSP [β -Ti(Fe,Sn) phase], have been estimated to be $\tau_{\beta\text{-Ti}} = 484.7$ MPa, $\tau_{\beta\text{-Ti(Fe,Sn)}} = 438.4$ MPa and $\tau_{\text{FeTi}} = 445.8$ MPa from the hardness measurements. Whereas, individual phases in $y = 0$ AMI and $y = 1$ AMI NECs such as pure-Ni [γ -Ni phase] and Ni_5Zr MSP [Ni_5Zr phase], and $\text{Ni}_{95}\text{Zr}_{0.4}\text{Al}_{4.6}$ MSP [γ -Ni(Zr,Al) phase] have been estimated to be $\tau_{\gamma\text{-Ni}} = 175.6$ MPa, $\tau_{\gamma\text{-Ni(Zr,Al)}} = 108.4$ MPa and $\tau_{\text{Ni}_5\text{Zr}} = 375.1$ MPa [13]. The required shear stress (τ_a) to activate slip in FeTi or Ni_5Zr due to the dislocation pile-up in β -Ti or γ -Ni, respectively have been estimated from the following relation: [10, 20]:

$$\tau_{shear} = \left(\frac{\tau_a - \tau_{CRSS}}{2} \right) \times \sqrt{\frac{L}{r}} \times \left[2\cos\frac{3\theta}{2} + \sin\theta \times \sin\frac{\theta}{2} \right] \quad (3)$$

where, L is the pile-up length, r is the distance from the tip of a pile-up to the location where these stresses are estimated, and θ ($\geq 0^\circ$) is the pile-up angle. It has been observed that the Sn addition has changed the lattice parameter of β -Ti without altering the lattice parameter of

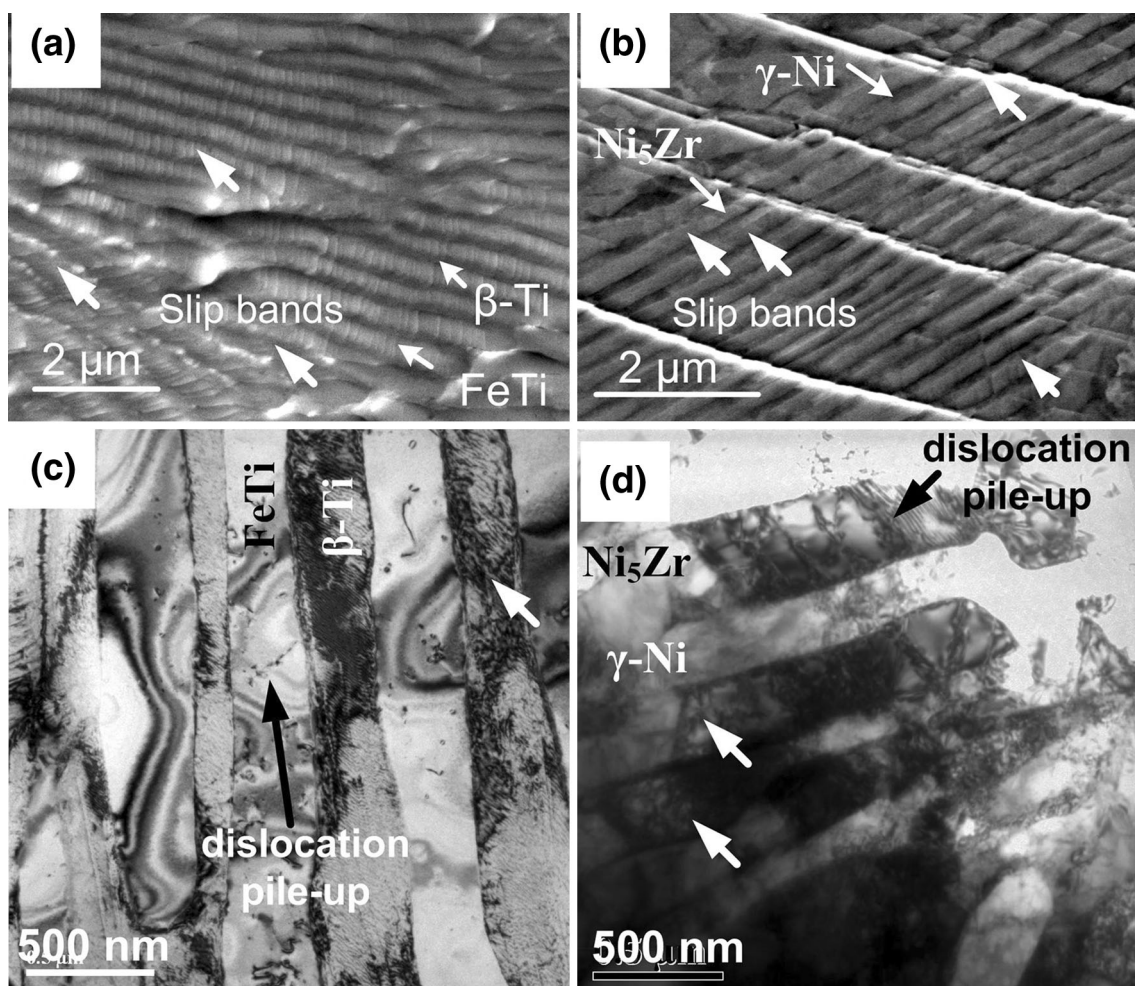


Fig. 5 SEM BSE image of deformed **a** $x = 3$ AMI ($\epsilon_p = 10\%$) and **b** $y = 1$ AMI ($\epsilon_p = 20\%$) NECs showing the evolution of the slip bands as marked by *arrows*. TEM BF image of **c** $x = 3$ AMI and **d** $y = 1$ AMI NECs showing the presence of dislocation pile-up at the β -Ti/FeTi and γ -Ni/Ni₅Zr interface

FeTi, which was also confirmed by EDS analysis under transmission electron microscope [15]. Therefore Sn preferentially dissolves in β -Ti without bringing any change to the structure of FeTi. Similar effect has been noticed in the case of Ni–Zr–(Al) where Al preferentially dissolves in γ -Ni only [11]. Therefore, ternary alloy addition such as Sn or Al alters neither the structure in terms of lattice parameter nor the chemistry of the intermetallic compounds, viz., FeTi and Ni₅Zr. Hence, alloy addition does not influence the cleavage surface energy of these intermetallic phases. On the other hand, the stress required to nucleate plasticity induced cleavage crack in brittle FeTi or Ni₅Zr due to the dislocation pile-up has been estimated as [10, 20]:

$$\sigma_{cleavage} = \left[\frac{2G\gamma_s}{L(1-\nu)\pi} \right]^{1/2} \quad (4)$$

where, G is shear modulus, γ_s is the cleavage surface energy of the hard intermetallic FeTi or Ni₅Zr, which is

considered as 4 J/mm^2 , ν is poisson's ratio, and L is the pile-up length which has been taken as 0.8 ($x = 0$ AMI) and 0.3 ($x = 3$ AMI) and 0.30 ($y = 0$ AMI) and $0.25 \mu\text{m}$ ($y = 1$ AMI), respectively [10]. The value of G has been estimated to be 87 and 68 GPa for FeTi and Ni₅Zr, respectively [10]. It has been estimated that in case of $x = 0$ AMI, the minimum shear stress required to activate slip in FeTi is 547.7 MPa , which is very close to the required stress (567.2 MPa) at which cleavage is predicted [10]. Whereas, the minimum shear stress required in the case of $x = 3$ AMI to cause slip in FeTi is 501.4 MPa , which is much lower than the stress (609.4 MPa) required for initiating cleavage [10]. Similarly, the minimum shear stress required to activate slip in Ni₅Zr is 228.65 MPa , which is very close to the required stress (268.42 MPa) at which cleavage is predicted in $y = 0$ AMI. Whereas, the minimum shear stress required in the case of $y = 1$ AMI to cause slip in Ni₅Zr is 161.45 MPa , which is much lower than the stress (229.96 MPa) required for initiating

cleavage. Hence, yielding occurred locally first at β -Ti(Fe,Sn) or γ -Ni(Zr,Al) lamellae followed by dislocations pile-up at the β -Ti/FeTi or γ -Ni/Ni₅Zr lamellae interfaces. This leads to the formation of large population of sessile dislocations resulting in significant work hardening. However, dislocation pile-ups in the β -Ti/or γ -Ni lead to slip before initiation of cleavage in FeTi/or Ni₅Zr, which is proposed to be the origin of the plasticity in NECs. The mathematical model shows that, addition of Sn to Ti–Fe–(Sn) and Al in Ni–Zr–(Al) increases the cleavage stress, and thus the dislocation slip transfers across bcc β -Ti/FeTi and fcc γ -Ni/Ni₅Zr interfaces easily, which is one of the criteria for developing the high strength nanoeutectic composites.

4 Summary

Eutectic composites comprising of β -Ti/FeTi nano-lamellae in Ti–Fe–(Sn) and γ -Ni/Ni₅Zr nano-lamellae in Ni–Zr–(Al) alloys, have been synthesized. Addition of Sn or Al refines the lamellar spacing. The m values of the developed NECs lie in the range of 0.007 and 0.009 as obtained from the strain rate jump tests at room temperature. TEM and SEM investigations reveals that the large plasticity and strain hardening are linked with the dislocation movement and their pile-ups at the lamellae interfaces. The refinement of the microstructure and the presence of the hard intermetallic phase strengthen the composites. Whereas, addition of Sn in Ti–Fe–(Sn) and Al in Ni–Zr–(Al) increases the cleavage stress and thus, slip transfers across the lamellae interfaces easily, which improves the global plasticity of the nanoeutectic composites.

Acknowledgments The authors thank P. Das, R. Kundu, S. Maity, and K. Sahoo for technical assistance. Financial support provided by

SRIC, IIT Kharagpur (SGIRG Grant), and Naval Research Board, Govt. of India (Grant No. NRB/4003/PG/357), are gratefully acknowledged.

References

- Woodcock T G, Kushy M, Mato S, Alcalá G, Thomas J, Loser W, Gebert A, Eckert J, and Schultz L, *Acta Mater* **53** (2005) 5141.
- Sun B B, Sui M L, Wang Y M, Li Y, He G, Eckert J, and Ma E, *Acta Mater* **54** (2006) 1349.
- Barbier D, Huang M X, and Bouaziz O, *Intermetallics* **35** (2013) 41.
- Das J, Kim K B, Baier F, Löser W, and Eckert J, *Appl Phys Lett* **87** (2005) 161907.
- Park J M, Sohn S W, Kim T E, Kim D H, Kim K B, and Kim W T, *Scr Mater* **57** (2007) 1153.
- Das J, Theissmann R, Löser W, and Eckert J, *J Mater Res* **25** (2010) 943.
- Kim J Y, Lee B W, Read D T, and Kwon D, *Scr Mater* **52** (2005) 353.
- Zhang L C, Lu H B, Mickel C, and Eckert J, *Appl Phys Lett* **91** (2007) 051906.
- Park J M, Kim T E, Sohn S W, Kim D H, Kim K B, Kim W T, and Eckert J, *Appl Phys Lett* **93** (2008) 031913.
- Maity T, and Das J, *AIP Adv* **2** (2012) 032175.
- Maity T, and Das J, *Intermetallics* **63** (2015) 51.
- Standard ASTM G129-00, *Standard practice for slow strain rate testing to evaluate the susceptibility of metallic materials to environmentally assisted cracking*, ASTM International, Conshohocken (2013).
- Wei Q, Cheng S, Ramesh K T, and Ma E, *Mater Sci Eng A* **381** (2004) 71.
- Young R A, *Introduction to Rietveld Method*, Oxford University Press, Oxford, UK (1993).
- Maity T, and Das J, *J Alloys Compd* **585** (2014) 54.
- Taylor G, *Prog Mater Sci* **36** (1992) 29.
- Elmustafa A A, and Stone D S, *J Mech Phys Solids* **51** (2003) 357.
- Maity T, Roy B, and Das J, *Acta Mater* **97** (2015) 170.
- Juhász A, Tasnadi P, Szaszvari P, and Kovacs I, *J Mater Sci* **21** (1986) 3287.
- Stroh A N, *Adv Phys* **6** (1957) 418.